Engineering and Technology
2015; 2(4): 220-234
Published online June 30, 2015 (http://www.aascit.org/journal/et)

American Association for Science and Technology

Keywords
Cebeci and Smith Model, Baldwin and Lomax Model, Jones and Launder Model, Launder and Sharma Model, Reynolds Averaged Navier-Stokes Equations, Algebraic and k-ε Turbulence Models

Received: June 5, 2015
Revised: June 13, 2015
Accepted: June 14, 2015

Assessment of Several Turbulence Models as Applied to Supersonic Flows in 2D – Part I

Edisson S. G. Maciel

Aeronautical Engineering Division, ITA (Aeronautical Technological Institute), SP, Brazil

Email address
edisavio@edissonsavio.eng.br

Citation
Edisson S. G. Maciel. Assessment of Several Turbulence Models as Applied to Supersonic Flows in 2D – Part I. *Engineering and Technology.* Vol. 2, No. 4, 2015, pp. 220-234.

Abstract
In the present work, the Van Leer flux vector splitting scheme is implemented to solve the two-dimensional Favre-averaged Navier-Stokes equations. The Cebeci and Smith and Baldwin and Lomax algebraic models and the Jones and Launder and Launder and Sharma k-ε two-equation models are used in order to close the problem. The physical problem under study is the supersonic flow around a simplified version of the VLS (Brazilian "Satellite Launcher Vehice") configuration. The results have demonstrated that the stagnation pressure ahead of the VLS configuration is better predicted by the Baldwin and Lomax turbulence model.

1. Introduction

Conventional non-upwind algorithms have been used extensively to solve a wide variety of problems ([1]). Conventional algorithms are somewhat unreliable in the sense that for every different problem (and sometimes, every different case in the same class of problems) artificial dissipation terms must be specially tuned and judicially chosen for convergence. Also, complex problems with shocks and steep compression and expansion gradients may defy solution altogether.

Upwind schemes are in general more robust but are also more involved in their derivation and application. Some upwind schemes that have been applied to the Euler equations are: [2-3]. Some comments about these methods are reported below:

[2] suggested an upwind scheme based on the flux vector splitting concept. This scheme considered the fact that the convective flux vector components could be written as flow Mach number polynomial functions, as main characteristic. Such polynomials presented the particularity of having the minor possible degree and the scheme had to satisfy seven basic properties to form such polynomials. This scheme was presented to the Euler equations in Cartesian coordinates and three-dimensions.

[3] emphasized that the [4] scheme had low computational complexity and low numerical diffusion when compared to other methods. They also mentioned that the original method had several deficiencies. It yielded pressure oscillations in the proximity of shock waves. Problems with adverse mesh and with flow alignment were also reported. [3] proposed a hybrid flux vector splitting approach which alternated between the [4] scheme and the [2] scheme, at the shock-wave regions. This strategy assured that strength shock resolution was clearly and well defined.

In relation to turbulent flow simulations, [5] applied the Navier-Stokes equations to transonic flows problems along a convergent-divergent nozzle and around the NACA 0012 airfoil. The [6] model was used to close the problem. Three algorithms were implemented: the [7] explicit scheme, the [8] implicit scheme and the [9] explicit scheme. The results have shown that, in general terms, the [7] and the [9] schemes have presented better solutions.

[10] have performed a study involving three different turbulence models. In this paper, the Navier-Stokes equations were solved applied to the supersonic flow around a simplified configuration of the Brazilian Satellite Launcher, VLS. The algebraic models of [11] and of [6] and the one-equation model of [12] were used to close the problem. The algorithms of [13] and of [3] were compared and presented good results.

In terms of two-equation models, [14] have presented a work that deals with such models applied to the solution of supersonic aerospace flow problems. The two-dimensional Navier-Stokes equations written in conservative form, employing a finite volume formulation and a structured spatial discretization were solved. The [2] algorithm, first order accurate in space, was used to perform the numerical experiments. Turbulence was taken into account using two k-ε turbulence models, namely: the [15-16] models. The steady state supersonic flow around a simplified version of the Brazilian Satellite Launcher, VLS, configuration was studied. The results have shown that the pressure field generated by the model of [16] was stronger than the respective one obtained with the model of [15], although the latter predicts more accurate aerodynamic coefficients in this problem. The model of [16] predicted less intense turbulence kinetic energy- and dissipation-rate profiles than the model of [15], yielding less intense turbulence fields.

In the present work, the [2] flux vector splitting scheme is implemented, on a finite-volume context. The two-dimensional Favre-averaged Navier-Stokes equations are solved using an upwind discretization on a structured mesh. The algebraic models of [11] and [6] and the k-ε two-equation models of [17] and [18] are used in order to close the problem. The physical problem under study is the supersonic flow around a simplified version of the VLS configuration. The implemented scheme uses a MUSCL procedure to reach second order accuracy in space. The time integration uses a Runge-Kutta method of five stages and is second order accurate. The algorithm is accelerated to the steady state solution using a spatially variable time step. This technique has proved excellent gains in terms of convergence rate ([19-20]).

The results have demonstrated that the model of [6] has predicted the best value of the stagnation pressure ahead of the VLS configuration.

2. Navier-Stokes Equations

The two-dimensional flow is modeled by the Navier-Stokes equations, which express the conservation of mass and energy as well as the momentum variation of a viscous, heat conducting and compressible media, in the absence of external forces. The Navier-Stokes equations are presented in their two-equation turbulence model formulation. For the algebraic models, these two-equations are neglected and the [2] algorithm is applied only to the original four conservation equations. The integral form of these equations may be represented by:

$$\partial/\partial t\int_V Q dV+\int_S\left[\left(E_e-E_v\right)n_x+\left(F_e-F_v\right)n_y\right]dS+\int_V G dV=0, \quad (1)$$

where Q is written for a Cartesian system, V is the cell volume, n_x and n_y are components of the unity vector normal to the cell boundary, S is the flux area, E_e and F_e are the components of the convective, or Euler, flux vector, E_v and F_v are the components of the viscous, or diffusive, flux vector and G is the source term of the two-equation models. The vectors Q, E_e, F_e, E_v and F_v are, incorporating a k-ε formulation, given by:

$$Q=\begin{Bmatrix}\rho\\ \rho u\\ \rho v\\ e\\ \rho k\\ \rho s\end{Bmatrix},\ E_e=\begin{Bmatrix}\rho u\\ \rho u^2+p\\ \rho uv\\ (e+p)u\\ \rho ku\\ \rho su\end{Bmatrix},\ F_e=\begin{Bmatrix}\rho v\\ \rho uv\\ \rho v^2+p\\ (e+p)v\\ \rho kv\\ \rho sv\end{Bmatrix},\ E_v=\begin{Bmatrix}0\\ t_{xx}+\tau_{xx}\\ t_{xy}+\tau_{xy}\\ f_x\\ \alpha_x\\ \beta_x\end{Bmatrix};F_v=\begin{Bmatrix}0\\ t_{xy}+\tau_{xy}\\ t_{yy}+\tau_{yy}\\ f_y\\ \alpha_y\\ \beta_y\end{Bmatrix},\text{and } G=\begin{Bmatrix}0\\ 0\\ 0\\ 0\\ G_k\\ G_s\end{Bmatrix}, \quad (2)$$

where the components of the viscous stress tensor are defined as:

$$\begin{aligned}t_{xx}&=\left[2\mu_M\,\partial u/\partial x-2/3\mu_M\left(\partial u/\partial x+\partial v/\partial y\right)\right]/Re\ ;\\ t_{xy}&=\mu_M\left(\partial u/\partial y+\partial v/\partial x\right)/Re;\\ t_{yy}&=\left[2\mu_M\left(\partial v/\partial y\right)-2/3\mu_M\left(\partial u/\partial x+\partial v/\partial y\right)\right]/Re.\end{aligned} \quad (3)$$

The components of the turbulent stress tensor (Reynolds stress tensor) are described by the following expressions:

$$\begin{aligned}\tau_{xx}&=\left[2\mu_T\,\partial u/\partial x-2/3\mu_T\left(\partial u/\partial x+\partial v/\partial y\right)\right]/Re-2/3\rho k;\\ \tau_{xy}&=\mu_T\left(\partial u/\partial y+\partial v/\partial x\right)/Re;\\ \tau_{yy}&=\left[2\mu_T\,\partial v/\partial y-2/3\mu_T\left(\partial u/\partial x+\partial v/\partial y\right)\right]/Re-2/3\rho k.\end{aligned} \quad (4)$$

Expressions to f_x and f_y are given below:

$$f_x=\left(t_{xx}+\tau_{xx}\right)u+\left(t_{xy}+\tau_{xy}\right)v-q_x\ ; \quad (5)$$

$$f_y = \left(t_{xy} + \tau_{xy}\right)u + \left(t_{yy} + \tau_{yy}\right)v - q_y, \qquad (6)$$

where q_x and q_y are the Fourier heat flux components and are given by:

$$q_x = -\gamma/\mathrm{Re}\left(\mu_M/\mathrm{Pr}_L + \mu_T/\mathrm{Pr}_T\right)\partial e_i/\partial x; \qquad (7)$$

$$q_y = -\gamma/\mathrm{Re}\left(\mu_M/\mathrm{Pr}_L + \mu_T/\mathrm{Pr}_T\right)\partial e_i/\partial y. \qquad (8)$$

The diffusion terms related to the k-ε equations are defined as:

$$\begin{aligned}\alpha_x &= 1/\mathrm{Re}\left(\mu_M + \mu_T/\sigma_k\right)\partial k/\partial x;\\ \alpha_y &= 1/\mathrm{Re}\left(\mu_M + \mu_T/\sigma_k\right)\partial k/\partial y;\end{aligned} \qquad (9)$$

$$\begin{aligned}\beta_x &= 1/\mathrm{Re}\left(\mu_M + \mu_T/\sigma_s\right)\partial s/\partial x;\\ \beta_y &= 1/\mathrm{Re}\left(\mu_M + \mu_T/\sigma_s\right)\partial s/\partial y.\end{aligned} \qquad (10)$$

In the above equations, ρ is the fluid density; u and v are Cartesian components of the velocity vector in the x and y directions, respectively; e is the total energy per unit volume; p is the static pressure; k is the turbulence kinetic energy; s is the second turbulent variable, which is the rate of dissipation of the turbulence kinetic energy (k-ε model) for this work; the t's are viscous stress components; τ's are the Reynolds stress components; the q's are the Fourier heat flux components; G_k takes into account the production and the dissipation terms of k; G_s takes into account the production and the dissipation terms of s; μ_M and μ_T are the molecular and the turbulent viscosities, respectively; Pr_L and Pr_T are the laminar and the turbulent Prandtl numbers, respectively; σ_k and σ_s are turbulence coefficients; γ is the ratio of specific heats; Re is the laminar Reynolds number, defined by:

$$\mathrm{Re} = \rho V_{REF} l_{REF}/\mu_M, \qquad (11)$$

where V_{REF} is a characteristic flow velocity and l_{REF} is a configuration characteristic length. The internal energy of the fluid, e_i, is defined as:

$$e_i = e/\rho - 0.5\left(u^2 + v^2\right). \qquad (12)$$

The molecular viscosity is estimated by the empiric Sutherland formula:

$$\mu_M = bT^{1/2}/\left(1 + S/T\right), \qquad (13)$$

where T is the absolute temperature (K), b = 1.458x10^{-6} Kg/(m.s.K$^{1/2}$) and S = 110.4 K, to the atmospheric air in the standard atmospheric conditions ([21]).

The Navier-Stokes equations are dimensionless in relation to the freestream density, ρ_∞, the freestream speed of sound, a_∞, and the freestream molecular viscosity, μ_∞. The system is closed by the state equation for a perfect gas:

$$p = (\gamma - 1)\left[e - 0.5\rho\left(u^2 + v^2\right) - \rho k\right], \qquad (14)$$

considering the ideal gas hypothesis. The total enthalpy is given by $H = (e + p)/\rho$.

3. Numerical Algorithm – Van Leer Scheme

The space approximation of the integral Equation (1) yields an ordinary differential equation system given by:

$$V_{i,j}\, dQ_{i,j}/dt = -R_{i,j}, \qquad (15)$$

with $R_{i,j}$ representing the net flux (residual) of the conservation of mass, conservation of momentum and conservation of energy in the volume $V_{i,j}$. The residual is calculated as:

$$R_{i,j} = R_{i,j-1/2} + R_{i+1/2,j} + R_{i,j+1/2} + R_{i-1/2,j}, \qquad (16)$$

with $R_{i+1/2,j} = R^{c}_{i+1/2,j} - R^{d}_{i+1/2,j}$, where the superscripts "c" and "d" are related to convective and diffusive contributions, respectively. The cell volume is given by:

$$\begin{aligned}V_{i,j} = {} & 0.5\left|\left(x_{i,j} - x_{i+1,j}\right)y_{i+1,j+1} + \left(x_{i+1,j} - x_{i+1,j+1}\right)y_{i,j} + \left(x_{i+1,j+1} - x_{i,j}\right)y_{i+1,j}\right| + \\ & 0.5\left|\left(x_{i,j} - x_{i+1,j+1}\right)y_{i,j+1} + \left(x_{i+1,j+1} - x_{i,j+1}\right)y_{i,j} + \left(x_{i,j+1} - x_{i,j}\right)y_{i+1,j+1}\right|\end{aligned} \qquad (17)$$

The convective discrete flux calculated by the AUSM scheme (Advection Upstream Splitting Method) can be understood as a sum of the arithmetical average between the right (R) and the left (L) states of the cell face (i+½,j), involving volumes (i+1,j) and (i,j), respectively, multiplied by the interface Mach number, plus a scalar dissipative term, as shown in [4]. Hence,

$$R_{i+1/2,j} = |S|_{i+1/2,j}\left\{\frac{1}{2}M_{i+1/2,j}\left(\begin{bmatrix}\rho a\\ \rho au\\ \rho av\\ \rho aH\\ \rho ak\\ \rho as\end{bmatrix}_L + \begin{bmatrix}\rho a\\ \rho au\\ \rho av\\ \rho aH\\ \rho ak\\ \rho as\end{bmatrix}_R\right) - \frac{1}{2}\varphi_{i+1/2,j}\left(\begin{bmatrix}\rho a\\ \rho au\\ \rho av\\ \rho aH\\ \rho ak\\ \rho as\end{bmatrix}_R - \begin{bmatrix}\rho a\\ \rho au\\ \rho av\\ \rho aH\\ \rho ak\\ \rho as\end{bmatrix}_L\right)\right\} + \begin{bmatrix}0\\ S_x p\\ S_y p\\ 0\\ 0\\ 0\end{bmatrix}_{i+1/2,j}, \qquad (18)$$

where $S_{i+1/2,j} = \left[S_x \quad S_y\right]^t_{i+1/2,j}$ defines the normal area vector for the surface (i+½,j). The normal area components S_x and S_y to each flux interface are given in Tab. 1. Figure 1 exhibits the computational cell adopted for the simulations, as well its respective nodes and flux interfaces.

Table 1. *Values of S_x and S_y.*

Surface	S_x	S_y
i,j-1/2	$\left(y_{i+1,j} - y_{i,j}\right)$	$\left(x_{i,j} - x_{i+1,j}\right)$
i+1/2,j	$\left(y_{i+1,j+1} - y_{i+1,j}\right)$	$\left(x_{i+1,j} - x_{i+1,j+1}\right)$
i,j+1/2	$\left(y_{i,j+1} - y_{i+1,j+1}\right)$	$\left(x_{i+1,j+1} - x_{i,j+1}\right)$
i-1/2,j	$\left(y_{i,j} - y_{i,j+1}\right)$	$\left(x_{i,j+1} - x_{i,j}\right)$

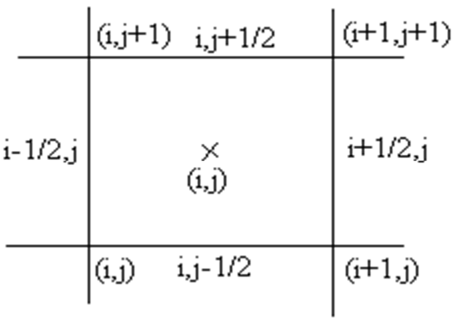

Figure 1. *Computational Cell.*

The quantity "a" represents the speed of sound, which is defined as:

$$a = \left(\gamma p/\rho - k\right)^{0.5}. \tag{19}$$

$M_{i+½,j}$ defines the advective Mach number at the (i+½,j) face, which is calculated according to [4]:

$$M_{i+1/2,j} = M_L^+ + M_R^-, \tag{20}$$

where the separated Mach numbers are defined by [2]:

$$M^+ = \begin{bmatrix} M, & \text{if } M \geq 1; \\ 0.25\left(M+1\right)^2, & \text{if } \left|M\right| < 1; \\ 0, & \text{if } M \leq -1; \end{bmatrix} \qquad M^- = \begin{bmatrix} 0, & \text{if } M \geq 1; \\ -0.25\left(M-1\right)^2, & \text{if } \left|M\right| < 1; \\ M, & \text{if } M \leq -1. \end{bmatrix} \tag{21}$$

M_L and M_R represent the Mach numbers associated with the left and the right states, respectively. The advection Mach number is defined by:

$$M = \left(S_x u + S_y v\right)/\left(a\left|S\right|\right). \tag{22}$$

The pressure at the face (i+½,j), related to the cell (i,j), is calculated by a similar formula:

$$p_{i+1/2,j} = p_L^+ + p_R^-, \tag{23}$$

with $p^{+/-}$ denoting the pressure separation and due to [2]:

$$p^+ = \begin{bmatrix} p, & \text{if } M \geq 1; \\ 0.25p\left(M+1\right)^2\left(2-M\right), & \text{if } \left|M\right| < 1; \\ 0, & \text{if } M \leq -1; \end{bmatrix} \tag{24a}$$

$$p^- = \begin{bmatrix} 0, & \text{if } M \geq 1; \\ 0.25p\left(M-1\right)^2\left(2+M\right), & \text{if } \left|M\right| < 1; \\ p, & \text{if } M \leq -1. \end{bmatrix} \tag{24b}$$

The definition of a dissipative term ϕ determines the particular formulation of the convective fluxes. The following choice corresponds to the [2] scheme, according to [3]:

$$\varphi_{i+1/2,j} = \varphi_{i+1/2,j}^{VL} = \begin{pmatrix} \left|M_{i+1/2,j}\right|, & \text{if } \left|M_{i+1/2,j}\right| \geq 1; \\ \left|M_{i+1/2,j}\right| + 0.5\left(M_R - 1\right)^2, & \text{if } 0 \leq M_{i+1/2,j} < 1; \\ \left|M_{i+1/2,j}\right| + 0.5\left(M_L + 1\right)^2, & \text{if } -1 < M_{i+1/2,j} \leq 0. \end{pmatrix} \tag{25}$$

The above equations clearly show that to a supersonic cell face Mach number, the [2] scheme represents a discretization purely upwind, using either the left state or the right state to the convective terms and to the pressure, depending of the Mach number signal. This [2] scheme is first order accurate in space. The time integration is performed using an explicit Runge-Kutta method of five stages, second order accurate, and can be represented in generalized form by:

$$\begin{aligned} Q_{i,j}^{(0)} &= Q_{i,j}^{(n)} \\ Q_{i,j}^{(k)} &= Q_{i,j}^{(0)} - \alpha_k \Delta t_{i,j}\left[R\left(Q_{i,j}^{(k-1)}\right)/V_{i,j} + G\left(Q_{i,j}^{(k-1)}\right)\right], \\ Q_{i,j}^{(n+1)} &= Q_{i,j}^{(k)} \end{aligned} \tag{26}$$

with k = 1,...,5; $\alpha_1 = 1/4$, $\alpha_2 = 1/6$, $\alpha_3 = 3/8$, $\alpha_4 = 1/2$ and $\alpha_5 =$ 1. The gradients of the primitive variables are calculated using the Green theorem, which considers that the gradient of a primitive variable is constant at the volume and that the volume integral which defines the gradient is replaced by a surface integral ([22]). To the $\partial u/\partial x$ gradient, for example, it is possible to write:

$$\begin{aligned} \frac{\partial u}{\partial x} &= \frac{1}{V}\int_V \frac{\partial u}{\partial x} dV = \frac{1}{V}\int_S u\left(\vec{n}_x \bullet d\vec{S}\right) = \frac{1}{V}\int_{S_x} u dS_x \\ &\cong \frac{1}{V}\Big[0.5\left(u_{i,j} + u_{i,j-1}\right)S_{x_{i,j-1/2}} + 0.5\left(u_{i,j} + u_{i+1,j}\right)S_{x_{i+1/2,j}} \\ &\quad + 0.5\left(u_{i,j} + u_{i,j+1}\right)S_{x_{i,j+1/2}} + 0.5\left(u_{i,j} + u_{i-1,j}\right)S_{x_{i-1/2,j}}\Big] \end{aligned}. \tag{27}$$

4. MUSCL Approach

Second order spatial accuracy can be achieved by introducing more upwind points or cells in the schemes. It has been noted that the projection stage, whereby the solution is projected in each cell face (i-1/2,j; i+1/2,j) on piecewise constant states, is the cause of the first order space accuracy of the Godunov schemes ([23]). Hence, it is sufficient to modify the first projection stage without modifying the Riemann solver, in order to generate higher spatial approximations. The state variables at the interfaces are thereby obtained from an extrapolation between neighboring cell averages. This method for the generation of second order upwind schemes based on variable extrapolation is often referred to in the literature as the MUSCL (Monotone Upstream-centered Schemes for Conservation Laws) approach. The use of nonlinear limiters in such procedure, with the intention of restricting the amplitude of the gradients appearing in the solution, avoiding thus the formation of new extrema, allows that first order upwind schemes be transformed in TVD high resolution schemes with the appropriate definition of such nonlinear limiters, assuring monotone preserving and total variation diminishing methods. Details of the present implementation of the MUSCL procedure are found in [24]. In this work, the minmod nonlinear limiter, defined in [23] and in [24], was employed in the numerical simulations.

5. Turbulence Models

5.1. Cebeci and Smith Turbulence Model

The problem of the turbulent simulation is in the calculation of the Reynolds stress. Expressions involving velocity fluctuations, originating from the average process, represent six new unknowns. However, the number of equations keeps the same and the system is not closed. The modeling function is to develop approximations to these correlations. To the calculation of the turbulent viscosity according to the model of [11], the boundary layer is divided in internal and external.

Initially, the (ν_w) kinematic viscosity at wall and the ($\tau_{xy,w}$) shear stress at wall are calculated. After that, the (δ) boundary layer thickness, the (δ_{LM}) linear momentum thickness and the (Vt_{BL}) boundary layer tangential velocity are calculated. So, the (N) normal distance from the wall to the studied cell is calculated. The N^+ term is obtained from:

$$N^+ = \sqrt{Re}\sqrt{\tau_{xy,w}/\rho_w}\,N/\nu_w\,, \tag{28}$$

where ρ_w is the wall density. The Van Driest damping factor is calculated by:

$$D = 1 - e^{(-N^+\sqrt{\rho/\rho_w}\,\mu_w/\mu/A^+)}\,, \tag{29}$$

with $A^+ = 26$ and μ_w is the wall molecular viscosity. After that, the (dVt/dN) normal to the wall gradient of the tangential velocity is calculated and the internal turbulent viscosity is given by:

$$\mu_{Ti} = Re\,\rho(\kappa ND)^2\,dVt/dN\,, \tag{30}$$

where κ is the von Kárman constant, which has the value 0.4. The intermittent function of Klebanoff is calculated to the external viscosity by:

$$g_{Kleb}(N) = \left[1 + 5.5(N/\delta)^6\right]^{-1}. \tag{31}$$

With it, the external turbulent viscosity is calculated by:

$$\mu_{Te} = Re(0.0168)\rho Vt_{BL}\delta_{LM}g_{Kleb}\,. \tag{32}$$

Finally, the turbulent viscosity is chosen from the internal and the external viscosities: $\mu_T = MIN(\mu_{Ti}, \mu_{Te})$.

5.2. Baldwin and Lomax Turbulence Model

To the calculation of the turbulent viscosity according to the model of [6], the boundary layer is again divided in internal and external. In the internal layer,

$$\mu_{Ti} = \rho l_{mix}^2\|\omega\| \quad \text{and} \quad l_{mix} = \kappa N\left(1 - e^{-N^+/A_0^+}\right). \tag{33}$$

In the external layer,

$$\mu_{Te} = \rho\alpha C_{cp}F_{wake}F_{Kleb}(N; N_{max}/C_{Kleb})\,, \tag{34}$$

with:

$$\begin{aligned} F_{wake} &= MIN\left[N_{max}F_{max}; C_{wk}N_{max}U_{dif}^2/F_{max}\right], \\ F_{max} &= 1/\kappa\left[\underset{N}{MAX}\left(l_{mix}\|\omega\|\right)\right] \end{aligned}. \tag{35}$$

Hence, N_{max} is the value of N where $l_{mix}\|\omega\|$ reached its maximum value and l_{mix} is the Prandtl mixture length. The constant values are: $\kappa = 0.4$, $\alpha = 0.0168$, $A_0^+ = 26$, $C_{cp} = 1.6$, $C_{Kleb} = 0.3$ and $C_{wk} = 1$. F_{Kleb} is the intermittent function of Klebanoff given by:

$$F_{Kleb}(N) = \left[1 + 5.5(C_{Kleb}N/N_{max})^6\right]^{-1}, \tag{36}$$

$\|\omega\|$ is the magnitude of the vortex vector and U_{dif} is the maximum velocity value in the boundary layer case. To free shear layers,

$$U_{dif} = \left(\sqrt{u^2+v^2}\right)_{max} - \left(\sqrt{u^2+v^2}\right)_{N=N_{max}}. \tag{37}$$

5.3. Jones and Launder Turbulence Model

In the turbulence model of [17], s = ε. To define the turbulent viscosity, or eddy viscosity, it is necessary to define the turbulent Reynolds number:

$$Re_T = k/(\nu_M\omega), \quad \text{with: } \nu_M = \mu_M/\rho \quad \text{and} \quad \omega = \varepsilon/k\,. \tag{38}$$

It is also necessary to determine the D damping factor:

$$D = e^{\left[-3.4/(1+0.02\,Re_T)^2\right]}. \quad (39)$$

The turbulent viscosity is expressed in terms of k and ω as:

$$\mu_T = Re\, C_\mu D\rho k/\omega, \quad (40)$$

with: C_μ a constant to be defined.

The source term denoted by G in the governing equation contains the production and dissipation terms of k and ε. To the model of [17], the G_k and G_ε terms have the following expressions:

$$G_k = -P_k - D_k \quad \text{and} \quad G_\varepsilon = -P_\varepsilon - D_\varepsilon, \quad (41)$$

where:

$$P = \left(\frac{\partial u}{\partial y} + \frac{\partial v}{\partial x}\right)\frac{\partial u}{\partial y},\; P_k = \left(\frac{C_\mu DP}{\omega^2}\right)\rho\omega k \Big/ Re; \quad (42)$$

$$D_k = \left[-\frac{2}{3}\left(\frac{\partial u}{\partial x} + \frac{\partial v}{\partial y}\right)\Big/\omega - \left(1 + \frac{2\nu_M}{\varepsilon}\frac{\partial k}{\partial y}\right)\right]\rho\omega k \Big/ Re; \quad (43)$$

$$P_\varepsilon = \left(\frac{C_{\varepsilon 1}C_\mu DP}{\omega^2}\right)\rho\omega\varepsilon \Big/ Re; \quad (44)$$

$$D_\varepsilon = \left[-\frac{2}{3}C_{\varepsilon 1}\left(\frac{\partial u}{\partial x} + \frac{\partial v}{\partial y}\right)\Big/\omega + 2C_\mu D\nu_M\left(\frac{\partial^2 u}{\partial y^2}\right)^2\Big/\omega^3 - C_{\varepsilon 2}E_f\right]\rho\omega\varepsilon \Big/ Re, \quad (45)$$

with the second damping factor E_f defined as: $E_f = 1 - 2/9\, e^{\left(-Re_T^2/36\right)}$. The closure coefficients adopted to the [17] model assume the following values: $\sigma_k = 1.0$; $\sigma_\varepsilon = 1.3$; $C_\mu = 0.09$; $C_{\varepsilon 1} = 1.45$; $C_{\varepsilon 2} = 1.92$; $Prd_L = 0.72$; $Prd_T = 0.9$.

5.4. Launder and Sharma Turbulence Model

The model of [18] also considers s = ε. The turbulent viscosity is defined by

$$\mu_T = Re\, C_\mu \rho k^2/\varepsilon, \quad (46)$$

with: C_μ a constant to be defined.

To the model of [18], the G_k and G_ε terms have the following expressions:

$$G_k = -P_k + D_k \quad \text{and} \quad G_\varepsilon = -P_\varepsilon + D_\varepsilon, \quad (47)$$

where:

$$P_k = \tau_{xy}\frac{\partial u}{\partial y}\Big/ Re \quad \text{and} \quad D_k = \rho\varepsilon; \quad (48)$$

$$P_\varepsilon = C_{\varepsilon 1}\varepsilon P_k/k \quad \text{and} \quad D_\varepsilon = C_{\varepsilon 2}\rho\varepsilon^2/k. \quad (49)$$

The closure coefficients adopted for the model of [18] are: $\sigma_k = 1.0$; $\sigma_\varepsilon = 1.3$; $C_\mu = 0.09$; $C_{\varepsilon 1} = 1.44$; $C_{\varepsilon 2} = 1.92$; $Prd_L = 0.72$; $Prd_T = 0.9$.

6. Spatially Variable Time Step

The basic idea of this procedure consists in keeping a constant CFL number in all calculation domain; thus allowing that appropriated time steps to each specific mesh region could be used during the convergence process. Hence, to a viscous simulation and according to the [25] work, it is possible to write:

$$\Delta t_{i,j} = \left(\frac{CFL(\Delta t_c \Delta t_v)}{\Delta t_c + \Delta t_v}\right)_{i,j}, \quad (50)$$

with Δt_c being the convective time step and Δt_v being the viscous time step. These quantities are defined as:

$$\begin{aligned}&(\Delta t_c)_{i,j} = \frac{V_{i,j}}{(\lambda_c)_{i,j}},\; (\lambda_c)_{i,j} = \max\left(\lambda^{max}_{i,j-1/2}, \lambda^{max}_{i+1/2,j}, \lambda^{max}_{i,j+1/2}, \lambda^{max}_{i-1/2,j}\right);\\ &\left(\lambda^{max}\right)_{int} = \left(\left|u_{int}n_x + v_{int}n_y\right| + a_{int}\right)S_{int},\end{aligned} \quad (51)$$

$$\begin{aligned}&(\Delta t_v)_{i,j} = K_v\frac{V_{i,j}}{(\lambda_v)_{i,j}},\; (p1)_{i,j} = \frac{\gamma^{3/2}M_\infty}{(Re\,Prd_L)V_{i,j}};\\ &(p2)_{i,j} = \frac{\mu_{i,j-1/2}}{\rho_{i,j-1/2}}S^2_{i,j-1/2} + \frac{\mu_{i+1/2,j}}{\rho_{i+1/2,j}}S^2_{i+1/2,j} + \frac{\mu_{i,j+1/2}}{\rho_{i,j+1/2}}S^2_{i,j+1/2} + \frac{\mu_{i-1/2,j}}{\rho_{i-1/2,j}}S^2_{i-1/2,j};\; ,\\ &(\lambda_v)_{i,j} = (p1 \times p2)_{i,j},\end{aligned} \quad (52)$$

where interface properties are calculated by arithmetical average, M_∞ is the freestream Mach number, μ is the fluid molecular viscosity and K_v is equal to 0.25, as recommended by [25].

7. Initial and Boundary Conditions

The initial and boundary conditions to the [6; 11] turbulence models are the same for perfect gas formulation. Details of these conditions can be found in [26-27]. For the k-ε, one has:

7.1. Initial Condition

Freestream values, at all grid cells, are adopted for all flow properties as initial condition, as suggested by [28-29]. Therefore, the vector of conserved variables is defined as:

$$Q_{i,j} = \left\{ 1 \quad M_\infty \cos\alpha \quad M_\infty \sin\alpha \quad \frac{1}{\gamma(\gamma-1)} + 0.5M_\infty^2 \quad f_1 K \quad f_2 K \right\}^t , \tag{53}$$

where α is the angle of attack, K is the kinetic energy of the mean flow and f_1 and f_2 are fractions. The kinetic energy of the mean flow is determined, considering the present dimensionless, as $K = 0.5M_\infty^2$. The values adopted for f_1 and f_2 in the present work were 0.005 and 0.2, respectively.

7.2. Boundary Conditions

The boundary conditions are basically of four types: solid wall, entrance, exit and far field. These conditions are implemented with the help of ghost cells.

(1) Wall condition: At a solid boundary the non-slip condition is enforced. Therefore, the tangent velocity component of the ghost volume at wall has the same magnitude as the respective velocity component of its real neighbor cell, but opposite signal. In the same way, the normal velocity component of the ghost volume at wall is equal in value, but opposite in signal, to the respective velocity component of its real neighbor cell.

The normal pressure gradient of the fluid at the wall is assumed to be equal to zero in a boundary-layer like condition. The same hypothesis is applied for the normal temperature gradient at the wall, assuming an adiabatic wall. The normal gradient of the turbulence kinetic energy at the wall is also assumed to be equal to zero.

From the above considerations, density, pressure and turbulence kinetic energy at the ghost volume are extrapolated from the respective values of its real neighbor volume (zero order extrapolation). The total energy is obtained by the perfect gas law and the rate of dissipation of the turbulence kinetic energy is determined by the following expression, considering production-destruction equilibrium:

$$(\rho\varepsilon)_{ghost} = C_\mu^{3/4} k_w^{3/2} \Big/ (0.41 d_n), \tag{54}$$

where k_w is the wall turbulence kinetic energy and d_n is the distance of the first mesh cell to the wall.

The properties of the first real volumes (j = 1) are necessary to be determined, aiming to guarantee that the u profile is correctly calculated by the numerical scheme. The u component of these cells is determined by the "wall law". It is initially necessary to calculate the wall shear stress, which is defined as:

$$\tau_w = \rho u C_\mu^{0.25} k_w^{0.5} \Big/ u^+ , \tag{55}$$

where u+ is defined as:

$$\begin{aligned} & u^+ = d^+, \quad d^+ < 5; \\ & u^+ = -3.05 + 5\ln d^+, \quad 5 \le d^+ < 30; \\ & u^+ = 5.5 + 2.5\ln d^+, \quad 30 \le d^+ < 2000, \end{aligned} \tag{56}$$

with: $d^+ = \rho C_\mu^{0.25} k_w^{0.5} d_n \big/ \mu_M$. The value of u of the real volume at the wall is obtained from:

$$u = d_n \tau_w \big/ \mu_M + u_{ghost} . \tag{57}$$

The v component is extrapolated from the ghost volume, with opposite signal, and the pressure is extrapolated from the real volume at j = 2. The turbulence kinetic energy is defined by its value at wall and the total energy of this volume is determined by the state equation for a perfect gas. The rate of dissipation of the turbulence kinetic energy to this volume is determined by Eq. (54).

(2) Entrance condition:

(2.1) Subsonic flow: Five properties are specified and one extrapolated. This approach is based on information propagation analysis along characteristic directions in the calculation domain ([29]). In other words, for subsonic flow, five characteristic propagate information pointing into the computational domain. Thus five flow properties must be fixed at the inlet plane. Just one characteristic line allows information to travel upstream. So, one flow variable must be extrapolated from the grid interior to the inlet boundary. The pressure was the extrapolated variable from the real neighbor volumes, for the studied problem. Density and velocity components adopted values of freestream flow. The turbulence kinetic energy and the rate of dissipation of the turbulence kinetic energy were fixed with the values of the initial condition, with the modification of $K = 0.5u^2$. The total energy is determined by the state equation of a perfect gas.

(2.2) Supersonic flow: In this case no information travels upstream; therefore all variables are fixed with their of freestream values.

(3) Exit condition:

(3.1) Subsonic flow: Five characteristic propagate information outward the computational domain. Hence, the associated variables should be extrapolated from interior information. The characteristic direction associated to the "(q_{normal}-a)" velocity should be specified because it points inward to the computational domain ([29]). In this case, the ghost volume pressure is specified from its initial value. Density, velocity components, the turbulence kinetic energy, and the rate of dissipation of the turbulence kinetic energy are extrapolated. The total energy is obtained from the state equation of a perfect gas.

(3.2) Supersonic flow: All variables are extrapolated from interior grid cells, as no flow information can make its way upstream. In other words, nothing can be fixed.

(4) Far field condition: The mean flow kinetic energy is assumed to be $K = 0.5u^2$ and the turbulence kinetic energy at the far field adopts the value $k_{ff} = 0.005K$, or 0.5% of K. The turbulence dissipation energy is assumed $\varepsilon_{ff} = 0.20K$ or 20% of K.

8. Results

Tests were performed in a Dual Core processor of 2.3GHz and 2.0Gbytes of RAM microcomputer. Three orders of reduction of the maximum residual in the field were considered to obtain a converged solution. The residual was defined as the value of the discretized conservation equation. The entrance or attack angle was adopted equal to zero. The ratio of specific heats, γ, assumed the value 1.4.

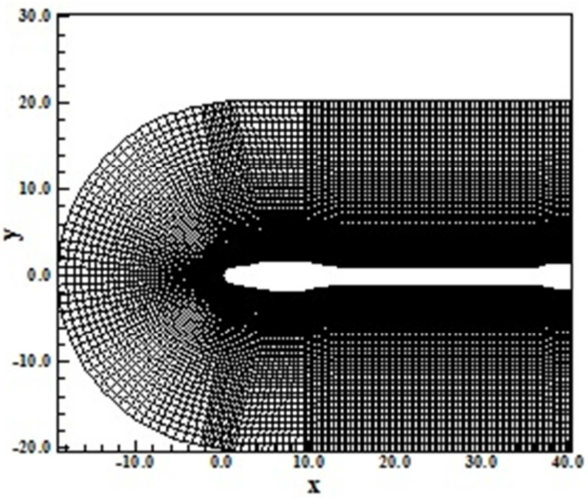

Figure 2. *VLS viscous mesh.*

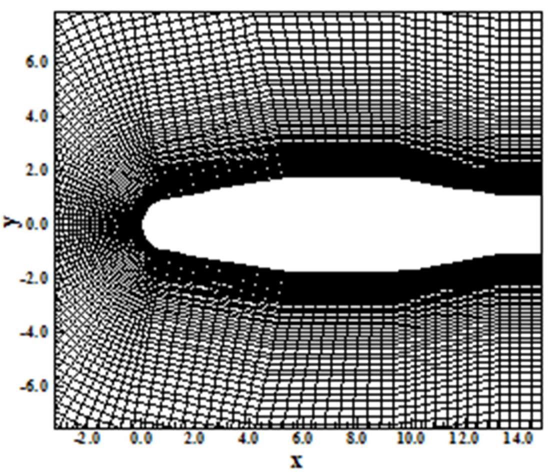

Figure 3. *Detail of the satellite compartment.*

Figures 2 shows the entire VLS viscous mesh, whereas Fig. 3 shows the detail of the VLS close to the satellite compartment. A mesh of 253x70 points or composed of 17,388 rectangular cells and 17.710 nodes was generated, employing an exponential stretching of 5% in the η direction.

The initial data of the simulations was described in Tab. 2.

Table 2. *Initial Conditions.*

M_∞	θ	Altitude	L_∞	Re
3.0	0.0°	40,000m	3.76m	8.93×10^5

8.1. Cebeci and Smith Results

Figure 4 exhibit the pressure contours obtained by the second order [2] scheme. The contours are uniform and well defined. The normal shock wave at the blunt body nose is well captured. Figure 5 exhibits the Mach number contours obtained by the high resolution TVD [2] scheme. The viscous region close to the VLS walls is well captured; in other words, the heat conduction, through the Fourier law, is well captured by the turbulence model. The normal shock weave is well captured. The solution is free of pre-shock oscillations.

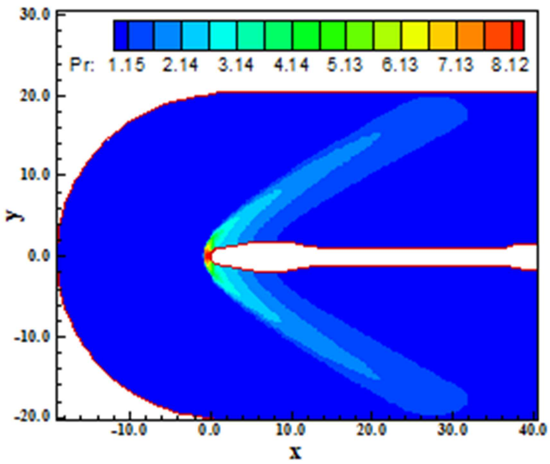

Figure 4. *Pressure contours (CS).*

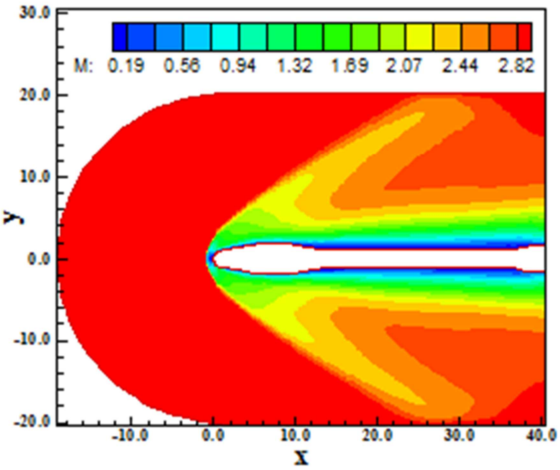

Figure 5. *Mach number contours (CS).*

Figure 6 presents the translational/rotational temperature contours obtained by the [2] scheme. Temperatures above 776.54 K are obtained. The region downstream the satellite compartment appears with regions of high dissipation, as can be noted in the figure. In other words, this means that circulation bubbles are formed as consequence of boundary layer displacement. These can be seen in Figs. 7 and 8, which highlight the circulation bubble formations downstream the satellite compartment.

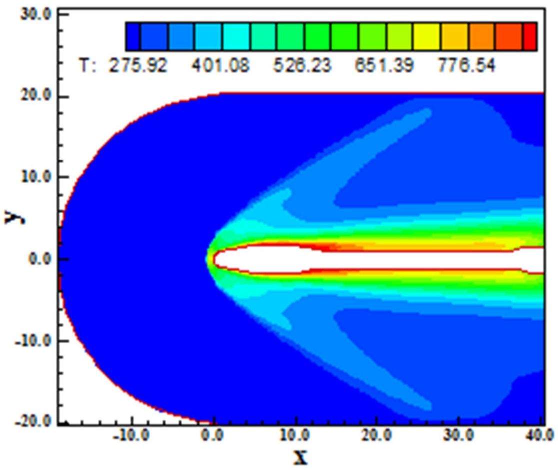

Figure 6. *Temperature contours (CS).*

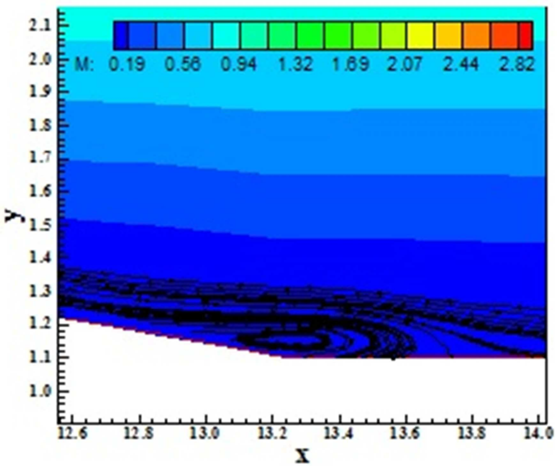

Figure 7. *Circulation bubble formation (right side-CS).*

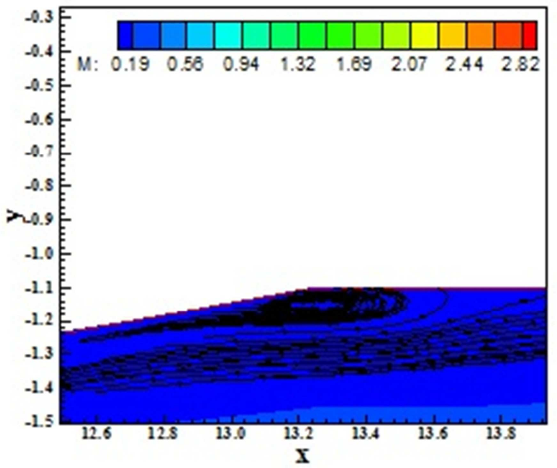

Figure 8. *Circulation bubble formation (left side-CS).*

Figure 9 shows the –Cp distribution along the blunt body wall. The Cp suffers a rapid increase at the satellite compartment and downstream it keeps horizontal. In all this distribution, no overshoots and undershoots are perceptible, even for a second-order scheme. This aspect highlights the MUSCL procedure as a good tool to provide clean profiles.

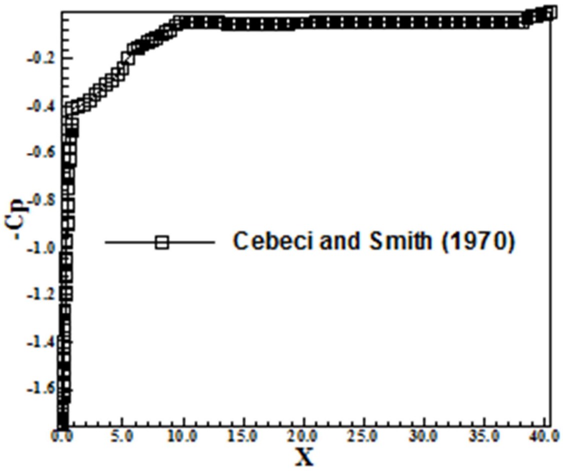

Figure 9. *–Cp distribution (CS).*

8.2. Baldwin and Lomax Results

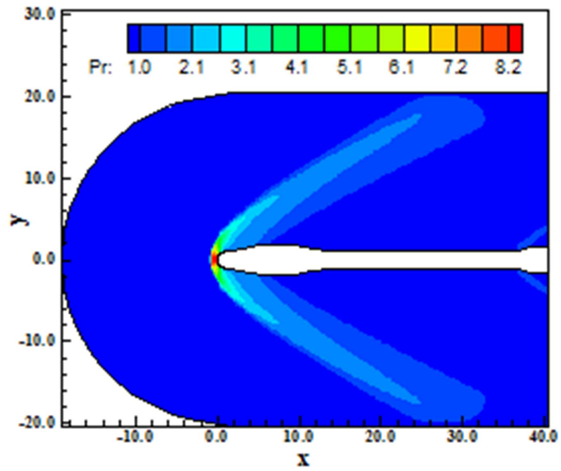

Figure 10. *Pressure contours (BL).*

Figure 10 shows the pressure contours obtained by the [2] scheme as using the turbulence model of [6]. The shock is well defined, better than that of the model of [11], as seen in Fig. 4, and homogeneous. As can be seen, there are qualitative differences between this plot and the corresponding plot of [11].

Figure 11 shows the Mach number contours obtained by the [2] scheme as using the turbulence model of [6]. As can see, the viscous region close to the VLS walls is well captured. The normal shock weave is also well captured. The solution is free of pre-shock oscillations.

Figure 12 exhibits the temperature field obtained by the [2] scheme as using the turbulence model of [6]. Qualitatively, this plot has differences in relation to the plot of [11], Fig. 6.

Qualitatively in terms of contours lines distribution, in terms of the heated region after the cockpit and in terms of the viscous layer aspect. Moreover, the regions of high dissipation are well spread out and temperatures close to 826.3 K are reached.

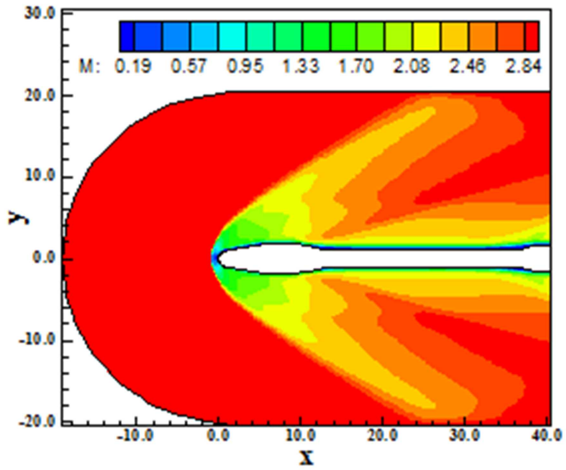

Figure 11. *Mach number contours (BL).*

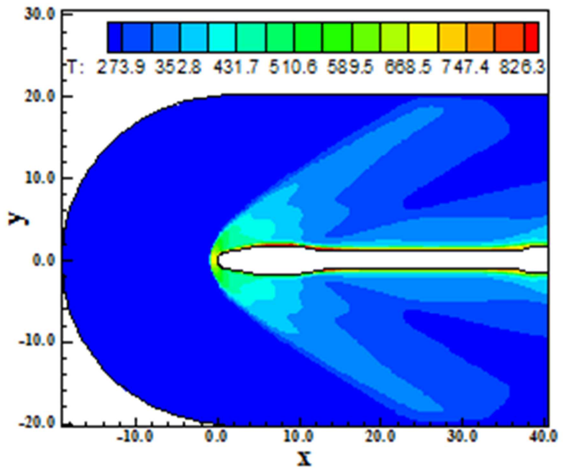

Figure 12. *Temperature contours (BL).*

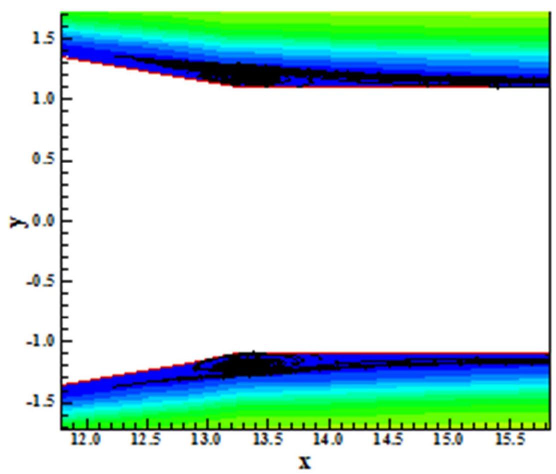

Figure 13. *Circulation bubble formation (Cockpit-BL).*

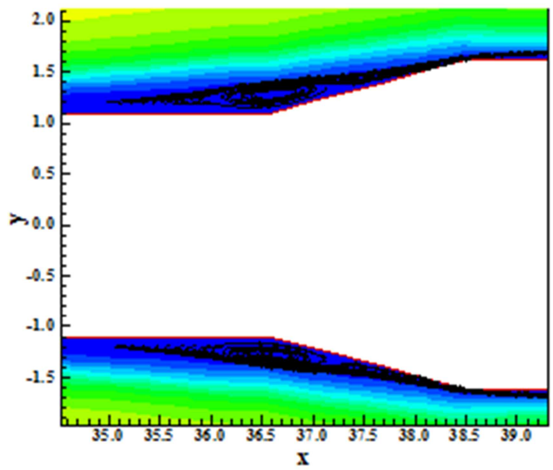

Figure 14. *Circulation bubble formation (Boosters-BL).*

Figures 13 and 14 show details of the cockpit and booster regions of the VLS. Both regions present small separation regions at the corner (cockpit) and at the ramp (boosters), causing the formation of separation bubbles. These figures are very interesting because show this flow separation.

Circulation bubbles are formed as the result of the boundary layer detachment, resulted from separation flow. A pair of vortices is formed as resulted of the high energy dissipation in these regions.

Figure 15 presents the –Cp distribution at wall of the VLS configuration, generated by the turbulence model of [6]. This curve presents a reduction of –Cp close to the boosters region and after that the pressure coefficient is recovered at the boosters' end. The entire –Cp distribution is more severe than the respect of the [11] model, see Fig. 9.

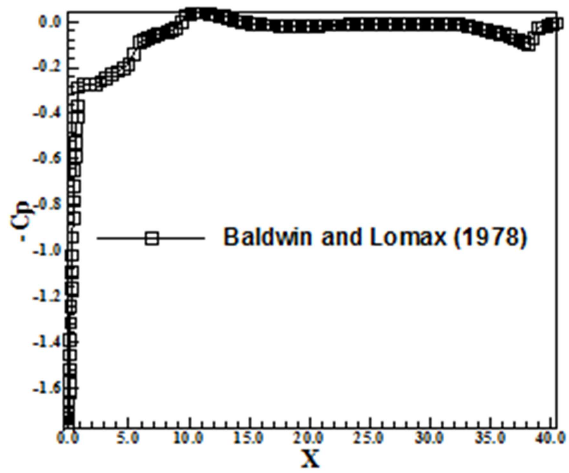

Figure 15. *–Cp distribution (BL).*

8.3. Jones and Launder Results

Figure 16 shows the pressure contours generated by the [2] scheme as using the [17] turbulence model. This curve is very similar to that obtained as using the model of [6], Fig. 10, and both indicate that the solution of [11], Fig. 4, is more dissipative than the formers. The shock is well captured and the solution is homogeneous, without pre-shock oscillations.

Figure 17 exhibits the Mach number contours obtained as using the turbulence model of [17]. The solution is very close to the solution of [6], Fig. 11, indicating the good performance of this algebraic turbulence model. They are very close in terms of contour line distributions and in terms of the subsonic regions detected at the end of the cockpit region and at the beginning of booster region. Regions of discrete formation of separation bubbles are perceptible at the downstream region of the satellite compartment and at the booster region. It is possible to see in Figs. 19 and 20, where circulation bubbles are well formed.

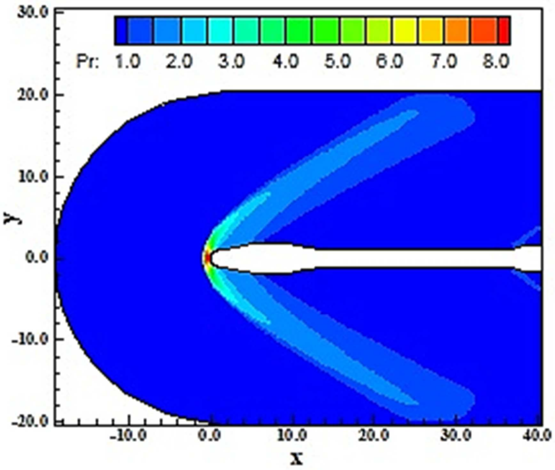

Figure 16. Pressure contours (JL).

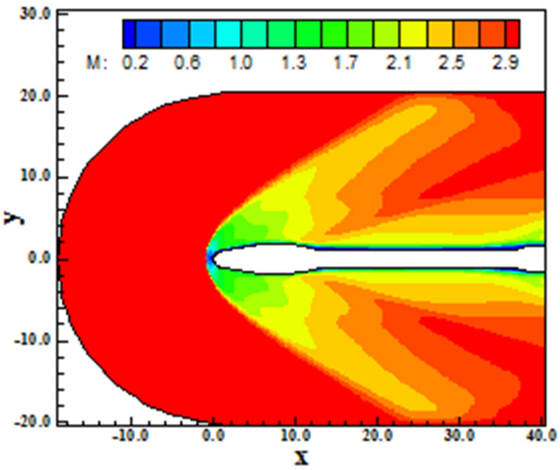

Figure 17. Mach number contours (JL).

Figure 18 presents the translational temperature contours originated by the [2] scheme as using the turbulence model of [6]. Temperatures near 691.7 K are observed in the field, but smaller than the results of [11] and [6], Figs. 6 and 12, respectively. Regions of high temperature are observed at the blunt body nose, at the satellite compartment end, and at the booster beginning. Figures 19 and 20 corroborate what was observed in the aforementioned paragraph. Circulation bubbles formation is originated at regions of high heating and generate loss of energy by the bubbles displacement and energy exchange due to collisions.

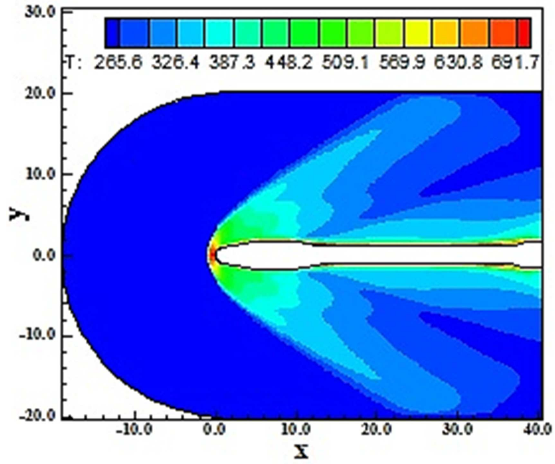

Figure 18. Temperature contours (JL).

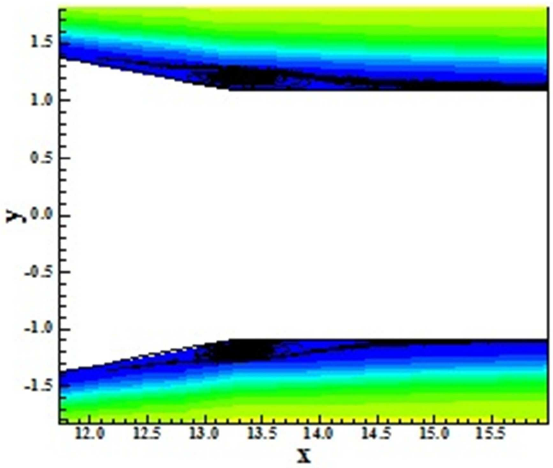

Figure 19. Circulation bubble formation (Cockpit-JL).

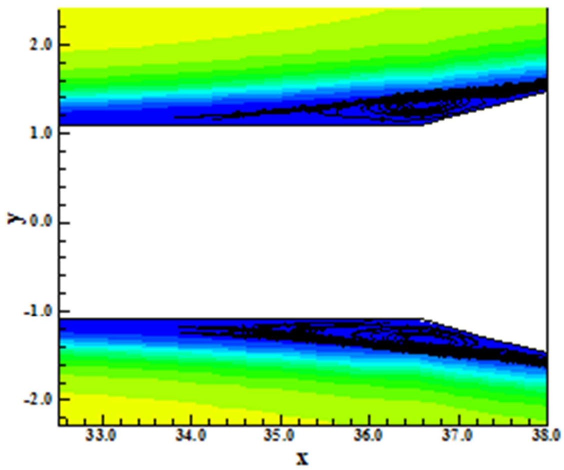

Figure 20. Circulation bubble formation (Boosters-JL).

Figure 21 exhibits the –Cp distribution originated by the turbulence model of [17]. The cockpit upstream region presents a pressure distribution in steps and also presents the reduction of pressure close to the boosters region, with the consequent increase of such pressure, obtained in the solution of [6].

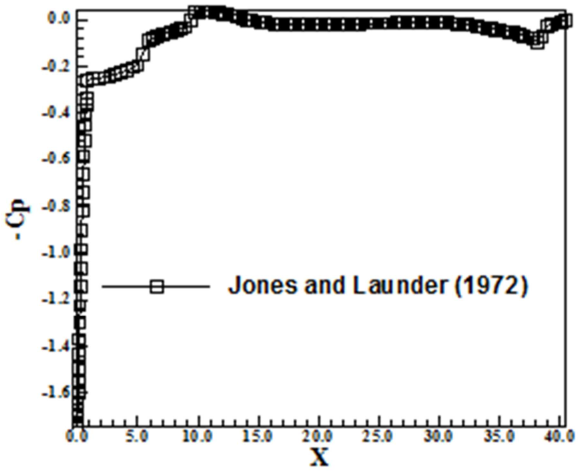

Figure 21. *–Cp distribution (JL).*

The –Cp profile of [17], Fig. 21, is more strength than the –Cp profile of the turbulence model of [11], Fig. 9, but is equivalent in qualitative and quantitative terms in relation to the turbulence model of [6], Fig. 15.

8.4. Launder and Sharma Results

Figure 22 shows the pressure contours obtained by the [2] algorithm as using the turbulence model of [18]. The curves of contours are well defined and dissipation is minimum, as is the case with the solutions of [6] and [17], Figs. 10 and 16, respectively.

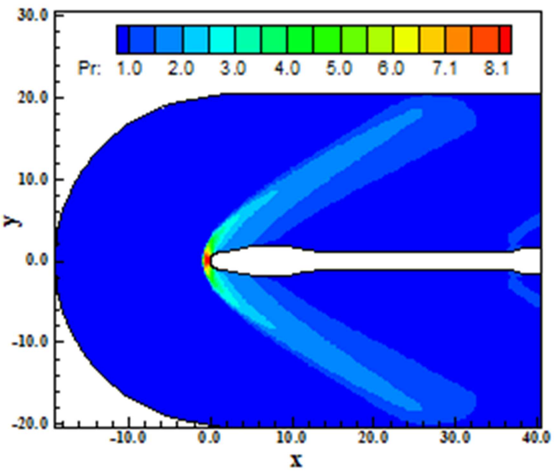

Figure 22. *Pressure contours (LS).*

No overshoots or undershoots are present. Figure 23 exhibit the Mach number contours obtained by the turbulence model of [18]. The contours are close to the solutions of [6] and [17], 11 and 17, respectively. No pre-shock oscillations are perceptible. The subsonic region is formed at the blunt nose as expected.

Figure 24 presents the translational temperature contours originated from the turbulence model of [18]. The temperature peak is observed near to 672.7 K, which is less than the captured fields of [6] and [17], Figs 12 and 18, respectively. It is not possible to detect regions of great heating near the satellite compartment end or at the booster regions. Ratifying this observation, no circulation bubble formation was observed in these regions.

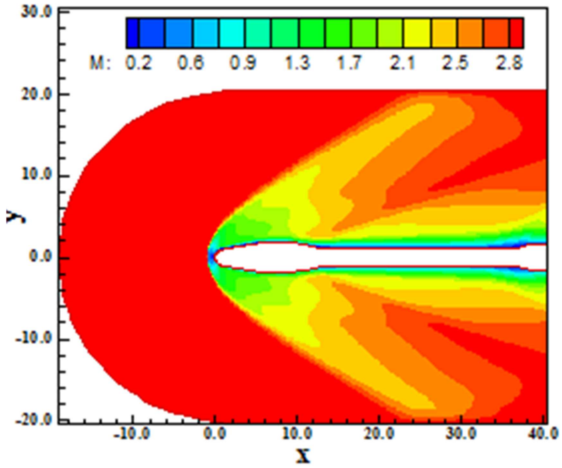

Figure 23. *Mach number contours (LS).*

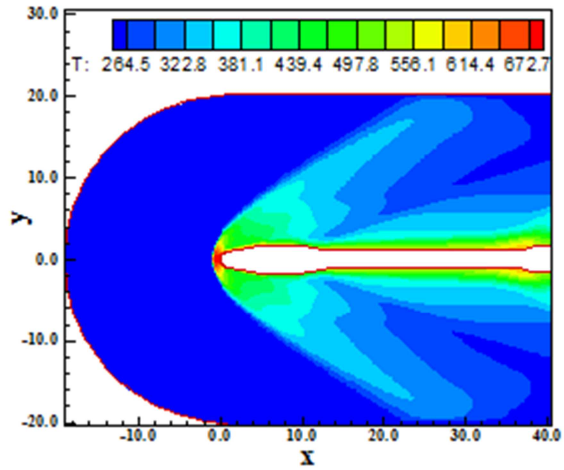

Figure 24. *Temperature contours (LS).*

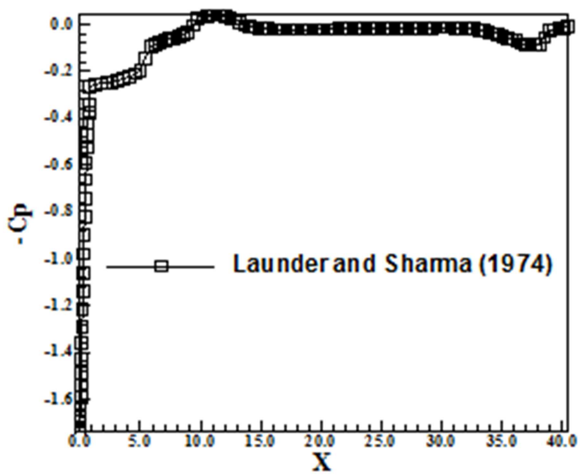

Figure 25. *–Cp distribution (LS).*

Figure 25 shows the –Cp distribution obtained with the turbulence model of [18]. The step profile at the blunt nose region and the hole region at the booster region are again observable. This –Cp profile is more strength than the profile of [11], Fig. 9.

As main conclusion of this four turbulence models studied herein, the models of [6], [17] and [18] are practically identical in qualitative terms. They present similar contour line distributions, capture similar zones of subsonic flow at the downstream region of the cockpit and at the upstream region of the boosters, and the main aspect of the flow field are well characterized. They gives more severe –Cp conditions than the model of [11], Fig. 9, and they gives less dissipative solutions. More severe conditions to –Cp because present higher values of –Cp at the VLS nose and capture the hole region close to the booster region. They are less dissipative than the model of [11] because capture, for example, the hole region at the booster region.

8.5. Quantitative Analysis

Table 3 shows the lift and drag aerodynamic coefficients calculated by the [2] scheme in the turbulent cases. As the geometry is symmetrical and an attack angle of zero value was adopted in the simulations, the lift coefficient should have a zero value.

Table 3. *Aerodynamic coefficients of lift and drag.*

Turbulence Model:	c_L:	c_D:
[11] turbulence model	$2.507\text{x}10^{-4}$	0.075
[6] turbulence model	$1.127\text{x}10^{-6}$	0.074
[17] turbulence model	$3.288\text{x}10^{-6}$	0.072
[18] turbulence model	$-1.773\text{x}10^{-6}$	0.072

The most correct value to the lift coefficient is due to the turbulence model of [6].

Another possibility to quantitative comparison of the laminar and turbulent cases is the determination of the stagnation pressure ahead of the configuration. [30] presents a table of normal shock wave properties in its B Appendix. This table permits the determination of some shock wave properties as function of the freestream Mach number. In front of the VLS configuration, the shock wave presents a normal shock behavior, which permits the determination of the stagnation pressure, behind the shock wave, from the tables encountered in [30]. So it is possible to determine the ratio pr_0/pr_∞ from [30], where pr_0 is the stagnation pressure in front of the configuration and pr_∞ is the freestream pressure (equals to $1/\gamma$ to the present dimensionless).

Table 4. *Values of the stagnation pressure and respective percentage errors.*

Turbulence Model:	pr_0:	Error (%):
[11] turbulence model	8.10	5.80
[6] turbulence model	8.20	4.70
[17] turbulence model	8.00	7.00
[18] turbulence model	8.10	5.80

Hence, to this problem, $M_\infty = 3.0$ corresponds to pr_0/pr_∞ = 12.06 and remembering that pr_∞ = 0.714, it is possible to conclude that pr_0 = 8.61. Values of the stagnation pressure to the turbulent cases and respective percentage errors are shown in Tab. 4. They are obtained from Figures 4, 10, 16, and 22. The percentage error is defined as:

$$\text{error}(\%) = \frac{|\text{Theoretical Value} - \text{Numerical Value}|}{\text{Theoretical Value}} \times 100 \,. \tag{58}$$

As can be observed, the turbulence model of [6] presents the best result, with a percentage error of 4.70%.

Finally, Table 5 exhibits the computational data of the present simulations. It can be noted that the most efficient is the [6] turbulence model.

Table 5. *Computational data.*

Turbulence Model:	CFL:	Iterations:
[11] turbulence model	0.10	6,415
[6] turbulence model	0.10	5,558
[17] turbulence model	0.10	7,602
[18] turbulence model	0.05	12,805

As final conclusion of this study, the turbulence model of [6] was the best when comparing these four turbulence models: [11], [6], [17] and [18]. It was proved by the good description of the flow filed in terms of qualitative aspects and by the good numerical results of lift coefficient and of the prediction of the stagnation pressure. In a next paper, the present author will study more four different turbulent models to this same problem trying to identify the best of each group of four and to perform a final analysis to found the best one.

As a final observation, the grid independence was not studied because this mesh of 253x70 points is a high density mesh and has presented the main aspects that were expected to capture in the flow field. Moreover, this mesh with an exponential stretching of 5.0% was employed in the study of fifteen different turbulence models and similar aspects of the flow field as: capture of the boundary layer and viscous layer, capture of the shock wave, capture of circulation bubble formations, were obtained in all cases.

9. Conclusions

In the present work, the [2] flux vector splitting scheme is implemented, on a finite-volume context. The two-dimensional Favre-averaged Navier-Stokes equations are solved using an upwind discretization on a structured mesh. The algebraic models of [11] and [6] and the k-ε two-equation models of [17] and [18] are used in order to close the problem. The physical problem under study is the supersonic flow around a simplified version of the VLS configuration. The implemented scheme uses a MUSCL procedure to reach second order accuracy in space. The time integration uses a Runge-Kutta method of five stages and is second order accurate. The algorithm is accelerated to the steady state solution using a spatially variable time step. This technique has proved excellent gains in terms of convergence rate as reported in [19-20].

The results have demonstrated that the model of [6] has yielded critical pressure fields, so intense than the ones of the other models. The stagnation pressure ahead of the VLS configuration is better predicted by the turbulence model of [6].

In a next paper, the present author will study more four different turbulent models to this same problem trying to identify the best of each group of four and to perform a final analysis to found the best one.

Acknowledgment

The author would like to thank the infrastructure of ITA that allowed the realization of this work.

References

[1] P. Kutler, “Computation of Three-Dimensional, Inviscid Supersonic Flows”, *Lecture Notes in Physics*, vol. 41, pp. 287-374, 1975.

[2] B. Van Leer, “Flux-Vector Splitting for the Euler Equations”, Proceedings of the 8th International Conference on Numerical Methods in Fluid Dynamics, E. Krause, Editor, *Lecture Notes in Physics*, vol. 170, pp. 507-512, Springer-Verlag, Berlin, 1982.

[3] R. Radespiel, and N. Kroll, “Accurate Flux Vector Splitting for Shocks and Shear Layers”, *Journal of Computational Physics*, vol. 121, pp. 66-78, 1995.

[4] M. Liou, and C. J. Steffen Jr., “A New Flux Splitting Scheme”, *Journal of Computational Physics*, vol. 107, pp. 23-39, 1993.

[5] E. S. G. Maciel, and N. G. C. R. Fico Jr., “Estudos de Escoamentos Turbulentos Utilizando o Modelo de Baldwin e Lomax e Comparação entre Algoritmos Explícitos e Implícitos”, *Proceedings of the III National Congress of Mechanical Engineering (III CONEM)*, Belém, PA, Brazil, 2004. [CD-ROM]

[6] B. S. Baldwin, and H. Lomax, “Thin Layer Approximation and Algebraic Model for Separated Turbulent Flows”, *AIAA Paper 78-257*, 1978.

[7] R. W. MacCormack, “The Effect of Viscosity in Hypervelocity Impact Cratering”, *AIAA Paper 69-354*, 1969.

[8] T. H. Pulliam, and D. S. Chaussee, “A Diagonal Form of an Implicit Approximate-Factorization Algorithm”, *Journal of Computational Physics*, vol. 39, pp. 347-363, 1981.

[9] A. Jameson, W. Schmidt, and E. Turkel, “Numerical Solution of the Euler Equations by Finite Volume Methods Using Runge-Kutta Time Stepping Schemes”, *AIAA Paper 81-1259*, 1981.

[10] E. S. G. Maciel, and N. G. C. R. Fico Jr., “High Resolution Algorithms Coupled with Three Turbulence Models Applied to an Aerospace Flow Problem – Part I”, *AIAA Paper 06-0292*, 2006. [CD-ROM]

[11] T. Cebeci, and A. M. O. Smith, “A Finite-Difference Method for Calculating Compressible Laminar and Turbulent Boundary Layers”, *Journal of Basic Engineering,* Trans. ASME, Series B, vol. 92, no. 3, pp. 523-535, 1970.

[12] P. R. Sparlat, and S. R. Allmaras, “A One-Equation Turbulence Model for Aerodynamic Flows”, *AIAA Paper 92-0439*, 1992.

[13] A. Harten, “High Resolution Schemes for Hyperbolic Conservation Laws”, *Journal of Computational Physics*, vol. 49, pp. 357-393, 1983.

[14] E. S. G. Maciel, and N. G. C. R. Fico Jr., “Comparação Entre Modelos de Turbulência de Duas Equações Aplicados a um Problema Aeroespacial”, *Proceedings of the Primer Congreso Argentino de Ingeniería Mecánica (I CAIM),* Bahía Blanca, Argentina, 2008. [CD-ROM]

[15] F. Jacon, and D. Knight, “A Navier-Stokes Algorithm for Turbulent Flows Using an Unstructured Grid and Flux Difference Splitting”, *AIAA Paper 94-2292*, 1994.

[16] Y. Kergaravat, and D. Knight, “A Fully Implicit Navier-Stokes Algorithm for Unstructured Grids Incorporating a Two-Equation Turbulence Model”, *AIAA Paper 96-0414*, 1996.

[17] W. P. Jones, and B. E. Launder, “The Prediction of Laminarization with a Two-Equation Model of Turbulence”, *International Journal of Heat and Mass Transfer*, vol. 15, pp. 301-304, 1972.

[18] B. E. Launder, and B. I. Sharma, “Application of the Energy Dissipation Model of Turbulence to the Calculation of Flow Near a Spinning Disc”, *Letters in Heat and Mass Transfer*, vol. 1, no. 2, pp. 131-138, 1974.

[19] E. S. G. Maciel, “Analysis of Convergence Acceleration Techniques Used in Unstructured Algorithms in the Solution of Aeronautical Problems – Part I”, *Proceedings of the XVIII International Congress of Mechanical Engineering (XVIII COBEM)*, Ouro Preto, MG, Brazil, 2005. [CD-ROM]

[20] E. S. G. Maciel, “Analysis of Convergence Acceleration Techniques Used in Unstructured Algorithms in the Solution of Aerospace Problems – Part II”, *Proceedings of the XII Brazilian Congress of Thermal Engineering and Sciences (XII ENCIT)*, Belo Horizonte, MG, Brazil, 2008. [CD-ROM]

[21] R. W. Fox, and A. T. McDonald, *Introdução à Mecânica dos Fluidos*, Ed. Guanabara Koogan, Rio de Janeiro, RJ, Brazil, 632 p, 1988.

[22] L. N. Long, M. M. S. Khan, and H. T. Sharp, “Massively Parallel Three-Dimensional Euler/Navier-Stokes Method”, *AIAA Journal*, vol. 29, no. 5, pp. 657-666, 1991.

[23] C. Hirsch, *Numerical Computation of Internal and External Flows – Computational Methods for Inviscid and Viscous Flows*, John Wiley & Sons Ltd, 691p, 1990.

[24] E. S. G. Maciel, “Extension of the Steger and Warming and Radespiel and Kroll Algorithms to Second Order Accuracy and Implicit Formulation Applied to the Euler Equations in Two-Dimensions – Theory”, *Proceedings of the VI National Congress of Mechanical Engineering (VI CONEM)*, Campina Grande, PB, Brazil, 2010. [CD-ROM]

[25] D. J. Mavriplis, and A. Jameson, “Multigrid Solution of the Navier-Stokes Equations on Triangular Meshes”, *AIAA Journal*, vol. 28, no. 8, pp. 1415-1425, 1990.

[26] E. S. G. Maciel, "Comparação entre os Modelos de Turbulência de Cebeci e Smith e de Baldwin e Lomax", *Proceedings of the 5th Spring School of Transition and Turbulence (V EPTT)*, Rio de Janeiro, RJ, Brazil, 2006. [CD-ROM]

[27] E. S. G. Maciel, "Estudo de Escoamentos Turbulentos Utilizando os Modelos de Cebeci e Smith e de Baldwin e Lomax e Comparação entre os Algoritmos de MacCormack e de Jameson e Mavriplis", *Proceedings of the 7th Symposium of Computational Mechanics (VII SIMMEC),* Araxá, MG, Brazil, 2006. [CD-ROM]

[28] A. Jameson, and D. Mavriplis, "Finite Volume Solution of the Two-Dimensional Euler Equationson a Regular Triangular Mesh", *AIAA Journal*, vol. 24, no. 4, pp. 611-618, 1986.

[29] E. S. G. Maciel, "Simulação Numérica de Escoamentos Supersônicos e Hipersônicos Utilizando Técnicas de Dinâmica dos Fluidos Computacional", *Doctoral Thesis*, ITA, CTA, São José dos Campos, SP, Brazil, 2002.

[30] J. D. Anderson Jr., *Fundamentals of Aerodynamics*, McGraw-Hill, Inc., EUA, 563p, 1984.